

Article

# Preparation and Catalytic Performance of Expanded Graphite for Oxidation of Organic Pollutant

Ruijia Lan <sup>1,\*</sup>, Wenbin Su <sup>1</sup> and Jitai Li <sup>2</sup>

<sup>1</sup> College of Chemistry and Material Science, Langfang Normal University, Langfang 065000, China; 1220317@lfnu.edu.cn

<sup>2</sup> College of Chemistry and Environmental Science, Hebei University, Baoding 071000, China; lijitai@hbu.edu.cn

\* Correspondence: 1220319@lfnu.edu.cn; Tel.: +86-0316-2188-370

Received: 5 March 2019; Accepted: 11 March 2019; Published: 19 March 2019



**Abstract:** A classic carbon material—expanded graphite (EG), was prepared and proposed for a new application as catalysts for activating peroxydisulfate (PDS). EG samples prepared at different expansion temperatures were characterized by X-ray diffraction (XRD), X-ray photoelectron spectroscopy (XPS), and other methods. It was observed that there existed a remarkable synergistic effect in the EG/PDS combined system to degrade Acid Red 97 (AR97). Unlike other carbon material catalysts,  $sp^2$  carbon structure may be the main active site in the catalytic reaction. The EG sample treated at 600 °C demonstrated the best catalytic activity for the activation of PDS. Degradation efficiency of AR97 increased with raising PDS dosage and EG loadings. The pH of aqueous solution played an important role in degradation and adsorption, and near-neutrality was the optimal pH in this research. It was assumed that the radical pathway played a dominant role in AR97 degradation and that oxidation of AR97 occurred in the pores and interface layer on the external surface of EG by  $SO_4^{\cdot-}$  and  $\cdot OH$ , generated on or near the surface of EG. The radical oxidation mechanism was further confirmed by electron paramagnetic resonance spectroscopy. The EG sample could be regenerated by annealing, and the catalytic ability was almost fully recovered.

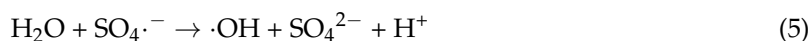
**Keywords:** sodium peroxydisulfate; expanded graphite; mechanism; degradation; acid red 97

## 1. Introduction

Recently, advanced oxidation processes (AOPs) based on sulfate radical ( $SO_4^{\cdot-}$ ) generated from peroxymonosulfate (PMS) and peroxydisulfate (PDS) have attracted much attention for the oxidation of water and soil contaminations. Sulfate radical has a higher oxidative potential ( $E^0 = 2.5\text{--}3.1$  V versus  $E^0 = 2.7$  V of hydroxyl radical), a longer lifetime ( $t_{1/2} = 30\text{--}40$   $\mu s$  of  $SO_4^{\cdot-}$  versus  $t_{1/2} \leq 1$   $\mu s$  of hydroxyl radical [1]), and a better flexibility of pH tolerance [2–4], which could be a promising alternative to the traditional hydroxyl radical. Analogous to hydroxyl radical, sulfate radicals could be obtained by activating persulfate through various homogeneous and heterogeneous activation processes. Transition metals (Fe(II), Zn(0), Fe(0)) catalysis [5–8] demonstrated the very simple and efficient homogeneous/ heterogeneous radical-based processes. On the other hand, heterogeneous processes with metal oxides or metal oxides-based catalysts, such as  $Fe_3O_4$ ,  $MnFe_2O_4$ ,  $Fe_3O_4/C/Mn$  hybrids, and  $\alpha\text{-}MnO_2$ , have drawn much attention recently due to their excellent performance [9–12]. The mechanism of activation of PDS and PMS by transition metal ions and metal oxide could be explained by Equations (1) and (2).



Nevertheless, the possible secondary pollution of these catalysts impeded their practical applications. Therefore, heterogeneous activation with metal-free catalysts is gaining popularity due to its many advantages, such as chemical stability and non-toxicity. Some carbonaceous materials, such as active carbon [13], mesoporous carbon [14], graphene oxide (GO) [15], reduced graphene oxide (rGO) [16], carbon nanotubes [17,18], and nanodiamond [19], have been employed as excellent metal-free catalysts and have shown great competitiveness in terms of avoiding metal toxics and associated contamination. The mechanism of electron conduction could account for the activation of PDS and PMS by carbonaceous-based materials. It was postulated that the  $sp^2$  covalent carbon network, oxygen-containing functional groups, and the defective edges conducted a redox cycle for electron transfer to persulphate to form radicals [14,20]. Thus, carbon materials could donate an electron to PMS or PDS to form the reactive radicals [21] (Equations (3) and (4)). Furthermore,  $SO_4^{\cdot-}$  in aqueous solution could react with  $H_2O$  or  $OH^-$  to produce  $\cdot OH$  (Equations (5) and (6)) [22]. Both  $SO_4^{\cdot-}$  and  $\cdot OH$  were responsible for the oxidation of organic contaminants in the system of persulphate activation [22].



The structural or chemical compositional modification of carbon materials could significantly improve the catalytic activity. Nitrogen doping [23,24] and sulfur doping [25] were commonly used modification methods. Besides  $sp^2$  carbon and the oxygen-containing functional groups, nitrogen and sulfur dopants also contributed to boost electron transfer. For the degradation of organics by persulfate activation, a non-radical mechanism has also been reported. In the research of Lee et al. [18], electron paramagnetic resonance spectroscopy (EPR) analyses suggested that  $SO_4^{\cdot-}$  and  $\cdot OH$  did not appear in the system. It was indicated that both persulfate and organics bound to the carbon material surface, and charge transfer complex was formed.

Expanded graphite (also known as exfoliated graphite, EG) was a kind of modified graphite that had a certain degree of separation of most of the carbon layers [26]. The expanded graphite was accordion-like or worm-like and had a large number of network-like pores in its structure. Expanded graphite consisted of stacked layers of  $sp^2$  hybridized carbon atoms bonded covalently in a hexagonal arrangement within the layer, and these layers were bonded to each other by weak van der Waals forces [27,28]. Many functional groups like carbonyl exist on the surface of EG. According to the structural features, we wonder if the EG could play similar roles to graphene in activating PDS. In this paper, EG material was prepared by the forming of ionic graphite intercalation compounds (GIC) (with sulfuric acid and nitric acid as intercalation reagents) [26], followed by thermal treatment of GIC.

Sun et al [16] first reported that reduced graphene oxide prepared by a hydrothermal method demonstrated an excellent catalytic ability to activate PMS for pollutant oxidation. Graphene oxide, graphitic oxide [29–31], and reduced graphene oxide [32] were often prepared by Hummers or a modified Hummers method, which needed a lot of oxidant ( $\text{mass}_{\text{potassium permanganate}}/\text{mass}_{\text{natural graphite}} \approx 3/1$ ), strict temperature conditions (e.g., ice bath and so on), and other complicated process and reagents. Compared with GO and rGO, the preparation of EG needed less oxidant, and the method was much simpler (as shown in Section 3.2.), which made EG material cost efficient.

Due to the structural features and economic advantages of EG, we decided to investigate the catalytic capacity of EG. As far as we know, although EG is often used as an adsorbent in environmental remediation [33–35], there is no report on using EG to activate peroxydisulfate for removing contaminants. In this paper, EG was prepared and applied as catalyst to catalytically oxidize organic dye Acid Red 97 (AR97) and the mechanism of PDS activation was discussed.

## 2. Results and Discussion

### 2.1. Materials Characterization

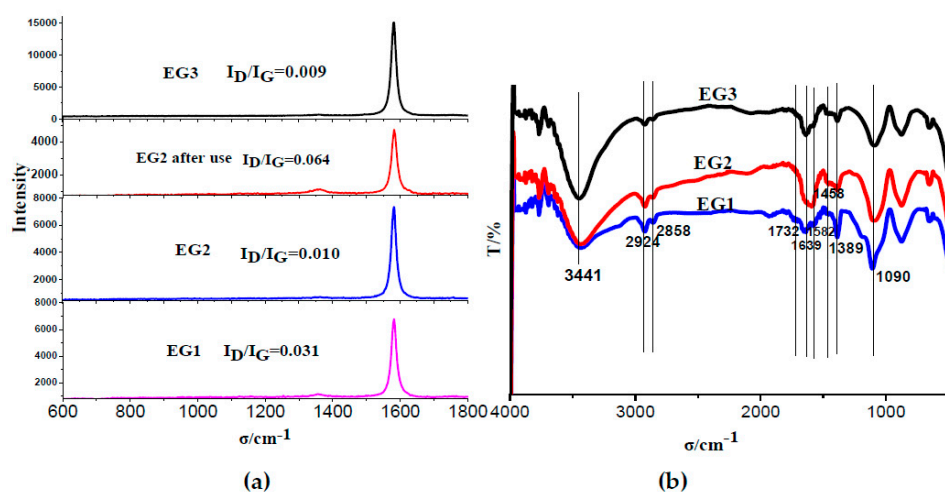
Scanning electron microscope (SEM) pictures and N<sub>2</sub> sorption isotherms of the EG samples can be seen in the Supplementary data of Figure S2.

Figure S3 shows XRD patterns of raw flake graphite, expandable graphite, and EG.

The sharp diffraction peaks at 26.51° and 26.21°, appearing in flake graphite and expandable graphite XRD patterns, suggest that oxidation and intercalation did not change the layered structure of the flake graphite, but the distance between the layers changed a little (from 0.336 to 0.340 nm). While for graphite oxide, prepared by various methods, spacing between the graphene layers varied from 0.7–0.8 nm [36]. XRD results proved that there was no graphite oxide formation in the intercalation process. Less oxidant (KMnO<sub>4</sub>) usage could explain the absence of graphene oxide. Due to the oxidation ability of KMnO<sub>4</sub> to open the graphite layers, the intercalating reagents could easily move into the layers to form GIC. When GIC was heated, intercalating reagents reacted with graphite, and then the formed gases would escape from the layer structures. The diffraction peak of expanded graphite appeared at about 26.67°. The value was very close to that of flake graphite and testified that the structure of the minimum composition of the expanded graphite—the carbon crystal layer—has not changed.

The intensity ratio I<sub>D</sub>/I<sub>G</sub> (strength of D band 1350 cm<sup>-1</sup> and G band 1580 cm<sup>-1</sup> in raman spectroscopy) was commonly used to characterize the defect density of carbon materials [37,38]. The I<sub>D</sub>/I<sub>G</sub> value gradually decreased from 0.031 to 0.009, with expansion temperature increasing from 300 to 800 °C, indicating that the EG prepared at a high temperature has good order and integrity. There may be two reasons for this: first, the intercalation reagents originally inserted between the layers were completely decomposed and escaped at a high temperature. Second, the EG was sufficiently annealed at a high temperature, and the structure has been improved [39]. It was worth noting that the I<sub>D</sub>/I<sub>G</sub> value of EG was much lower than that of graphene (I<sub>D</sub>/I<sub>G</sub> > 1) [32], sulfur-doped hierarchically porous carbon (~1) [25], and mesoporous carbon (1.2) [40].

The Fourier transform infrared (FTIR) spectrums of expanded graphites are shown in Figure 1b. The characteristic peaks at 2924, 2858 and 1458 cm<sup>-1</sup> were attributed to methene [41]. The characteristic peak at 1732 cm<sup>-1</sup> was ascribed to C=O stretching vibration, originating from the oxidization by KMnO<sub>4</sub> [42]. The peak at 1582 cm<sup>-1</sup> was contributed by the C=C stretching vibration in the graphite carbon hexagonal ring [37], indicating that carbon atoms were still tightly packed in a hexagonal structure. The peak at 1389 cm<sup>-1</sup> was for nitrogen groups [43]. As for the peak in the range of 1000 to 1100 cm<sup>-1</sup>, it might be the sum peak of S-O and C-O [44].



**Figure 1.** (a) Raman spectra and (b) The Fourier transform infrared (FTIR) spectra of expanded graphite (EG).

XPS information is derived from several to a dozen atomic layers on the surface of the EG sample, which can be used to analyze the composition (Table S1) and chemical states of elements on the surface of the sample (Figure 2). Table S1 shows that the higher the preparation temperature, the lower the oxygen, sulfur, and nitrogen content of EG samples. This result fully illustrates that the intercalation reagents between the layers were completely decomposed and escaped at a high temperature, which was consistent with the results of Raman spectra. A broad C1s peak of EG samples could be fitted into five species with binding energies at 284.79, 285.60, 286.80, 289.00 and 291.20 eV, which were assigned to carbon atoms with  $sp^2$  hybridization, C-O and/or C-S, C=O (carbonyl or quinone), O=C-O (carboxyl or ester), and  $\pi-\pi^*$  shake up, respectively [25,40] (Figure 2a–c correspond to EG1, EG2 and EG3, respectively). As mentioned above, the  $I_D/I_G$  value of EG was much lower than other carbon material activator. This result was confirmed by the XPS analyses. The percentage of C-C/C-H in other carbon catalysts was hierarchically porous carbon 53.83% [25], mesoporous carbon 47.10% [40], MWCNT 64.17% [14], and rGO 62.65% [14], whereas it was 75% in EG, which suggests that the graphitic crystalline structure was not obviously damaged.

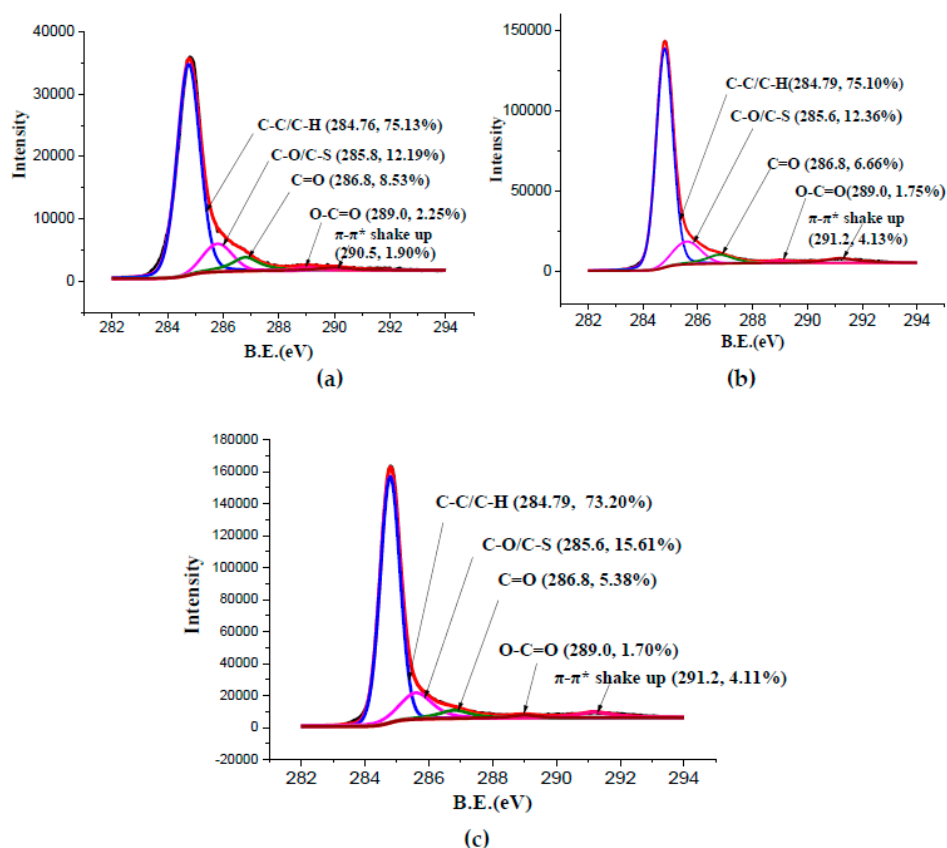


**Figure 2.** X-ray photoelectron spectroscopy (XPS) survey (C1s scan) of (a) EG1, (b) EG2, and (c) EG3.

## 2.2. Decolorization of AR97 in Different Systems

AR97 could be adsorbed by EG or it could be oxidized by PDS, as shown in Figure 3a. Within 80 min, only 16.7% AR97 was adsorbed by the sole EG system and only 2.4% AR97 was oxidized by the sole PDS system. However, nearly 94.6% AR97 was degraded by the PDS/EG combined system within 80 min. 94.6% was greater than the sum of 16.7 and 2.4%. Therefore, it was obvious that there was a remarkable synergistic effect in the EG/PDS combined system. This result was similar to the rGO/persulfate [16,32] or activated carbon /persulfate combined system studied by Zhang and Yang [45,46]. Therefore, it could be concluded that EG was also an excellent catalyst to activate persulfate decomposition and further induce the degradation of dye at an ambient temperature. The  $sp^2$  carbon and the electron-rich functional group might all be active sites in catalyst [47]. As shown

in Figure 2, compared with other catalysts, EG had a lower functional group content, but had more  $sp^2$  carbon, so  $sp^2$  carbons may be the main active sites in the catalytic reaction. The catalysis would be carried out with donated electrons from EG to PDS for producing  $SO_4^{\cdot-}$ .  $SO_4^{\cdot-}$  could be partly converted to  $\cdot OH$ . The generated  $SO_4^{\cdot-}$  and  $\cdot OH$  would then take part in the oxidation of AR97.

Some other carbon materials were also investigated for degradation of AR97, and the results are shown in Figure 3b. There are two strongly polar sulfonic acid groups in the molecule of AR97, as shown in Figure S1. Within 80 min, 91.2% AR97 was removed by the sole Multiwall Carbon Nanotubes (MWCNT) system, which meant that AR97 was strongly adsorbed on MWCNTs. A plausible explanation for the strong adsorption capacity was the polar surface of MWCNTs [48,49]. Meanwhile, 98.4% AR97 was removed by the MWCNTs/PDS combined system within 80 min. The result showed that MWCNTs/PDS system did not exhibit the remarkable synergistic effect, similar to EG/PDS. The rGO/PDS combined system did not manifest the synergistic effect, because 93.0% AR97 was removed by rGO and 99.7% AR97 was removed by the combined system within 80 min. The superior adsorption performance may be attributed to the large specific surface area of rGO, which was more than  $500 \text{ m}^2 \times \text{g}^{-1}$ .

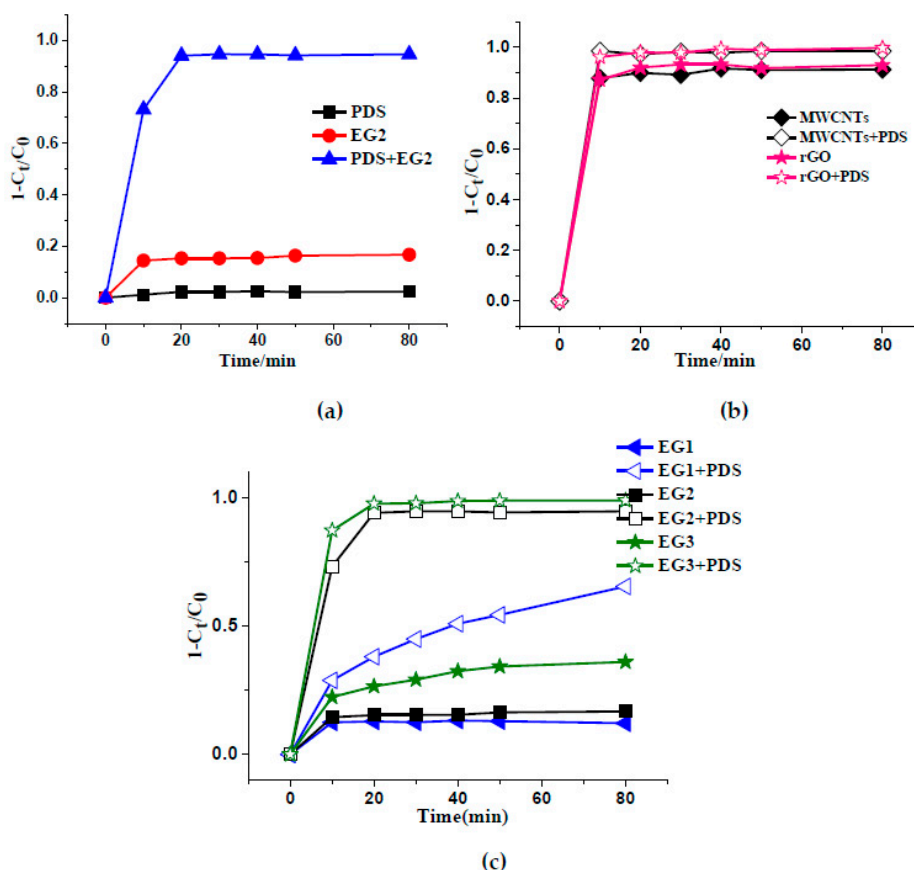


**Figure 3.** (a) Time-dependent degradation of Acid Red 97 (AR97) by EG2/PDS system, (b) Time-dependent degradation of AR97 by other catalyst/PDS systems, (c) The removal of AR97 under different EG.  $[AR97]_0 = 50 \text{ mg} \times \text{L}^{-1}$ ;  $[PDS]_0 = 2 \text{ mmol} \times \text{L}^{-1}$ ;  $\text{pH} = 6.9$ ;  $[EG1]_0 = 1 \text{ g} \times \text{L}^{-1}$ ;  $[EG2]_0 = 1 \text{ g} \times \text{L}^{-1}$ ;  $[EG3]_0 = 1 \text{ g} \times \text{L}^{-1}$ ;  $[CNT]_0 = 1 \text{ g} \times \text{L}^{-1}$ ;  $[rGO]_0 = 1 \text{ g} \times \text{L}^{-1}$ .

### 2.3. The Adsorptive and Catalytic Performances of Different EG Samples

Figure 3c depicts the adsorptive and catalytic performances of different EG samples by AR97 removal. In the adsorption tests, about 12.2, 16.7 and 36.0% of AR97 were removed by EG1, EG2 and EG3, respectively. Accordingly, their expansion volumes were 123, 221 and  $300 \text{ mL} \times \text{g}^{-1}$  and the specific surface areas (SSA) were 6.682, 45.798 and  $72.430 \text{ m}^2 \times \text{g}^{-1}$  (Table S1). Therefore, it could be

concluded that the adsorption abilities of the EG samples were in accordance with their expansion volumes and specific surface area.

While in the catalytic tests, by deducting their respective adsorption contributions, about 53.2, 77.9 and 62.8% of extra AR97 were removed by EG1, EG2 and EG3 in 80 min, respectively. Based on the aforementioned experimental results, it could be concluded that: firstly, the larger the specific surface area, the stronger the adsorption capacity, and EG3 showed the best adsorption capacity; secondly, the sample EG2 exhibited the best activation potential for PDS. As the expansion temperature increased, the relative content of C=O and O–C=O species decreased, while that of C–O increased (Figure 2). This indicated that during the high temperature treatment, some of the oxygen-containing functional groups were decomposed and rearranged (C=O and O–C=O were converted to C–O) [50]. C=O played a role in promoting the reaction of catalyzing PMS and PDS [47,50]. Although EG1 had the highest content of C=O (8.53%) among the three samples, it did not exhibit the best catalytic activity. The low catalytic activity of EG1 may be attributed to the lowest proportion (1.90%) of delocalized  $\pi$  electrons, which also play an important role in activating PDS. The small specific surface area also explained the poor catalytic performance of EG1. The portions of C=O and O–C=O species in EG3 were similar to those of EG2, but EG3 had a larger specific surface area. Compared to EG2, more of the active sites on EG3 were covered by dye molecule, and the electron transfer process was blocked, leading to the deactivation of EG3.

The Raman spectrum of EG2 after use is also shown in Figure 1a. The  $I_D/I_G$  value of EG2 increased from 0.01 to 0.064 after the reaction, which was more than six times that of the original, which indicated that the EG surface got oxidized during the reaction. The Raman spectrum of EG3 after use was also scanned (data not shown) and the  $I_D/I_G$  value (0.011) was almost unchanged after the reaction.

To see the catalytic activity of the two materials further, the decomposition of PDS was investigated. The apparent decomposition rate constants of PDS on EG2 and EG3 were  $5.9 \times 10^{-3}$  and  $4.25 \times 10^{-3} \text{ min}^{-1}$ , respectively. The higher decomposition rate constant of EG2 also proved that the sample EG2 exhibited the best catalytic potential for PDS.

#### 2.4. Effect of EG Dosage and PDS Concentration on AR97 Removal

Figure 4a shows the effect of EG dosage on the AR97 removal ratio by the EG/PDS system. With the increase of EG, the rate of bleaching was enhanced in both the EG-only system and the EG/PDS combined system. The more EG was used, the larger the number of active sites for adsorption and the activation of PDS could be achieved. There also existed a synergistic effect at a dosage of 2.0 g/L, however the effect was not as remarkable as the effect at the dosage of 1.0 g/L. The same result also occurred in the work of Yang [46], when the dosage of granular activated carbon reached 5 g/L, the synergistic effect of the degradation began to decline.

Figure 4b suggests that 11.5, 41.7, 82.68, 94.6 and 95.0% of AR97 was removed by the EG/PDS combined system, with the concentration of PDS of  $1 \times 10^{-5}$ ,  $1 \times 10^{-4}$ ,  $1 \times 10^{-3}$ ,  $2 \times 10^{-3}$ ,  $2.5 \times 10^{-2} \text{ mol} \times \text{L}^{-1}$ , respectively. Within the range of  $1 \times 10^{-5}$ – $2 \times 10^{-3} \text{ mol} \times \text{L}^{-1}$ , it was clear that a higher concentration of PDS significantly resulted in the increase of AR97 removal. This was mainly because a larger dosage of PDS could provide more reactive radicals for reaction. However, when the concentration of PDS increased from  $2.0 \times 10^{-3}$  to  $2.5 \times 10^{-2} \text{ mol} \times \text{L}^{-1}$ , no obvious increase of degradation efficiency was observed (from 94.6 to 95.0%) and the growth trend of rate constant  $k$  has slowed down (inset graph). It was reported that  $\text{SO}_4^{\cdot-}$ , produced by decomposition of PDS, can react with superfluous PDS to form  $\text{SO}_4^{2-}$  [51,52]. According to the work of Zhang [45], the decomposition efficiency of oxone decreased as the oxone concentration increased. Thus, it is not appropriate to use excessive oxidant to degrade AR97.

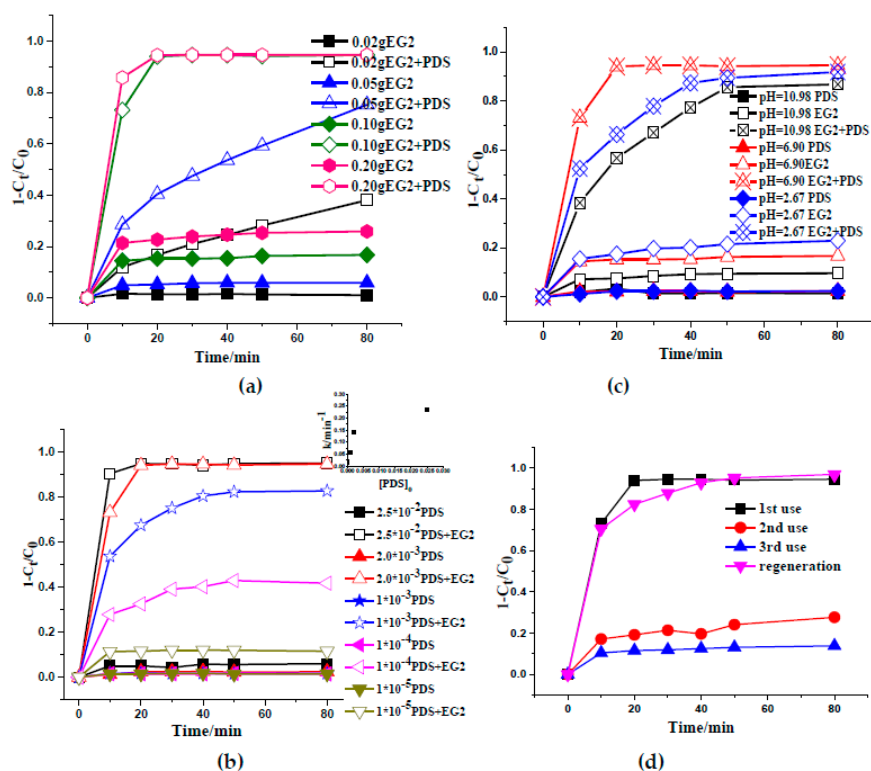


**Figure 4.** The effects of (a) catalyst dosage, (b) peroxydisulfate (PDS) dosage, (c) initial pH on AR97 removal, and (d) EG reuse in the EG/PDS combined system.  $[AR97]_0 = 50 \text{ mg} \times \text{L}^{-1}$ ;  $[PDS]_0 = 2 \text{ mmol} \times \text{L}^{-1}$ ;  $[EG2]_0 = 1 \text{ g} \times \text{L}^{-1}$ ;  $\text{pH} = 6.9$ .

### 2.5. Effect of Initial pH

Figure 4c depicts the influence of initial pH of AR97 aqueous solution. The highest removal efficiency of AR97 in the single EG adsorption system occurred at an initial pH of 2.67, but that occurred at initial pH 6.90 in the EG/PDS combined system. The adsorption capacity of EG increased with the decrease of the initial pH of solution. The  $\text{pH}_{\text{PZC}}$  of EG2 was about 6.00. The surface of EG was positively charged when  $\text{pH} (2.67) < \text{pH}_{\text{PZC}}$  and had a strong affinity for anionic dye AR97. However, when  $\text{pH} (10.98) > \text{pH}_{\text{PZC}}$ , the EG surface with negative charge repelled anionic dye AR97. The results of AR97 degradation in the presence of PDS differed from adsorption. The order of degradation efficiency of AR97 at different initial pH was: (initial pH 6.90) > (initial pH 2.67) > (initial pH 10.98). EG adsorbed more AR97 molecules on its surface in an acidic medium, and the oxidant itself could not effectively diffuse into pores occupied by organics [53]. However, when there was less adsorbate on the EG surface in an alkaline environment, the ratio of AR97 degradation was lower as well. This may be because the higher pH could lead to more negative charged sites on the EG surface, which kept the  $\text{S}_2\text{O}_8^{2-}$  and dye anions away from it [24]. Therefore, near-neutrality was the optimal initial pH for the AR97 degradation in the EG/PDS combined system.

### 2.6. Reuse of EG

The reuse test was carried out to detect the stability of EG2. Fresh EG could oxidize 94.6% of dyes in 80 min, and 27.7 and 13.9% of AR97 removals were achieved in 80 min in the second and third runs, respectively (Figure 4d). It implied that the EG was obviously deactivated after employment. This could be due to the decline of specific surface area ( $30.199 \text{ m}^2 \times \text{g}^{-1}$ ), which resulted in a poor adsorption capacity and a degradation efficiency on AR97. Similar results also appeared in Guo's research [25], in which the SSA of sulfur-doped hierarchically porous carbon significantly decreased after use. The regeneration of expanded graphite after catalyzing was also explored, and the results

showed that the catalytic ability of EG was almost 100% restored, with around 96.9% AR97 removal in 80 min.

### 2.7. Quenching Experiments and Radical Mechanism

To disclose the activation mechanism in the EG/PDS system, radical capturing reaction was utilized to investigate the effects of radicals.  $\text{SO}_4^{\cdot-}$  and  $\cdot\text{OH}$  are often considered as reactive species for the destruction of organic contaminants in PDS activation. Methanol (MeOH), containing  $\alpha$ -hydrogen, can be an effective quencher for both  $\text{SO}_4^{\cdot-}$  and  $\cdot\text{OH}$  [54], while *tert*-butanol (TBA) is only effective for  $\cdot\text{OH}$ , but not for  $\text{SO}_4^{\cdot-}$  [55].

Figure 5a shows that MeOH could impede the AR97 degradation with a decrease of  $k_{\text{obs}}$  from 0.1011 to 0.0404  $\text{min}^{-1}$  (inset graph). The inhibitory effect of TBA was stronger because the  $k_{\text{obs}}$  declined to 0.0362  $\text{min}^{-1}$ . These results suggest that both  $\text{SO}_4^{\cdot-}$  and  $\cdot\text{OH}$  were responsible for AR97 degradation in the EG/PDS system.

Phenol is another strong quencher of  $\text{SO}_4^{\cdot-}$  and  $\cdot\text{OH}$  radicals [56,57] and exerts a much stronger inhibiting effect than MeOH and TBA in the EG/PDS systems. As shown in Figure 5, the AR97 degradation almost stalled in the presence of phenol. The magnitude of the inhibition effect was in the order of phenol > TBA > MeOH. It was also testified that the presences of three inhibitors had very little effects on AR97 removal by the only EG adsorption (Figure 5b). PDS activated by carbon material belonged to the heterogeneous activation, and EG was a kind of hydrophobic carbon material with macro and mesopores [58,59]. The static water contact angle was measured to evaluate hydrophobic character of the surface of EG2. The surface contact angle was 105.743° (Figure S4), which proved that the surface of EG2 was hydrophobic. While MeOH and TBA are hydrophilic compounds, they cannot accumulate in large numbers on the EG surface and should rather react with  $\text{SO}_4^{\cdot-}$  and  $\cdot\text{OH}$  radicals in the bulk liquid. Phenol, with stronger hydrophobicity, is easier to approach the EG surface and can react with a large number of free radicals which were generated, and existed in, close proximity to the EG surface. As a result, in our experiments, the areas where the free radicals reacted with AR97 were most likely the pores or the interface layer on the external surface of EG [45,46].

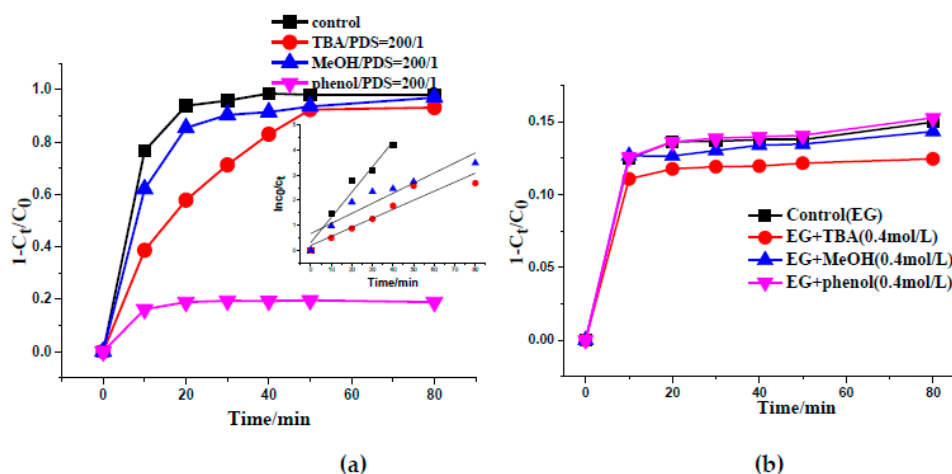


**Figure 5.** (a) Degradation and (b) adsorption of AR97 in the presence of different radical scavengers.  $[\text{AR97}]_0 = 50 \text{ mg} \times \text{L}^{-1}$ ;  $[\text{PDS}]_0 = 2 \text{ mmol} \times \text{L}^{-1}$ ;  $[\text{EG2}]_0 = 1 \text{ g} \times \text{L}^{-1}$ ;  $\text{pH} = 6.9$ ;  $[\text{TBA}]_0 = 0.4 \text{ mol} \times \text{L}^{-1}$ ;  $[\text{MeOH}]_0 = 0.4 \text{ mol} \times \text{L}^{-1}$ ;  $[\text{phenol}]_0 = 0.4 \text{ mol} \times \text{L}^{-1}$ .

To sum up the aforementioned capture reagent experiments, the activation mechanism of PDS by EG was radical mechanism and the proposed pathway of AR97 degradation might be: (I) PDS diffused from liquid phase into the pore dispersed on EG surface, (II) PDS decomposition was activated by EG, i.e., the electrons transferred from  $\text{sp}^2$  carbon structure and functional groups to PDS, and  $\text{SO}_4^{\cdot-}$  and  $\cdot\text{OH}$  were generated, as presented in Equations (3) and (5), (III) The radicals oxidized the AR97, and

AR97 was degraded into small molecule compounds, (IV) As PDS and AR97 near the surface of the catalyst were continuously consumed, the PDS and AR97 in the bulk solution continuously diffused to the surface of the catalyst and a diffusion–reaction cycle was formed. The proposed mechanism is shown in Figure 6.

Radical mechanism was further proved by the adsorption isotherms of AR97 on EG. For adsorption isotherms, Langmuir (Equation (7)) and Freundlich (Equation (8)) isotherm equations were selected to describe the adsorption:

$$\frac{1}{q_e} = \frac{1}{C_e q_0 b} + \frac{1}{q_0} \quad (7)$$

$$\log q_e = \log K_f + \frac{1}{n} \log C_e \quad (8)$$

$q_e$  (mg/g) and  $C_e$  (mg/L) were the equilibrium adsorption capacity and aqueous phase concentrations, respectively.  $q_0$  (mg/g) was the maximum capacity of adsorbate,  $b$  (L/mg) was the Langmuir constant.  $K_f$  was the Freundlich equilibrium constant and  $n$  was the nonlinearity factor.

All the fitting results of adsorption isotherms are listed in Tables S2 and S3. The Langmuir isotherm equation fitted better than the Freundlich isotherm equation for the present system and the maximum capacity of adsorbate and the Langmuir constant were calculated (Table S2). The  $q_0$  was 11.01~13.99 mg/g, and  $b$  was 0.06341~0.06757 L/mg. All of them were small. According to Pang's research [60], the dye holding a small  $b$  should have a weaker affinity between itself and expanded graphite. In their research, Langmuir constants for Basic Fuch sine (0.112 L/mg), Acid Brilliant Red 3B (0.032 L/mg), and Auramine Lake Yellow O (0.141 L/mg) were calculated, and the one for Acid Brilliant Red 3B was the smallest. The results were mainly caused by polar sulfo-group in the molecule of Acid Brilliant Red 3B [60]. Similar results were found in this study. Within 80 min, only 16.7% AR97 was adsorbed by the sole EG system (Figure 3). There are two strongly polar sulfonic acid groups in the molecule of AR97, while the surface of EG material is hydrophobic. Hence, the adsorption of AR97 on the expanded graphite was not the key factor in the oxidation of AR97 and the radical mechanism was further proved. In other words, the catalysis would be carried out with donated electrons from EG to PDS for producing  $\text{SO}_4^{\cdot-}$  and  $\cdot\text{OH}$ . The generated  $\text{SO}_4^{\cdot-}$  and  $\cdot\text{OH}$  would then take part in the oxidation of AR97.

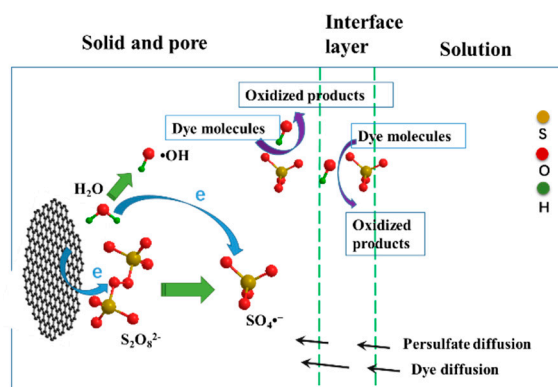


**Figure 6.** Simplified reaction pathways for AR97 degradation by EG/PDS system.

### 2.8. Electron Paramagnetic Resonance (EPR) Studies

EPR studies were carried out to verify the catalytic oxidation mechanism and identify the reactive species of EG/PDS system for AR97 degradation. As shown in Figure 7, the signals of DMPO-OH and DMPO-SO<sub>4</sub> were clearly seen [61], and the radicals oxidation mechanism was further confirmed. Ten minutes after the reaction began, the intensities of radical peaks reached their maximum. Both SO<sub>4</sub><sup>•-</sup> and  $\cdot\text{OH}$  manifested a receding after the first 10 min, ascribed to the consumption of AR97

oxidation, and showed no obvious change afterwards. This could be due to the stability of EG, which could continuously activate PDS during the whole reaction process.

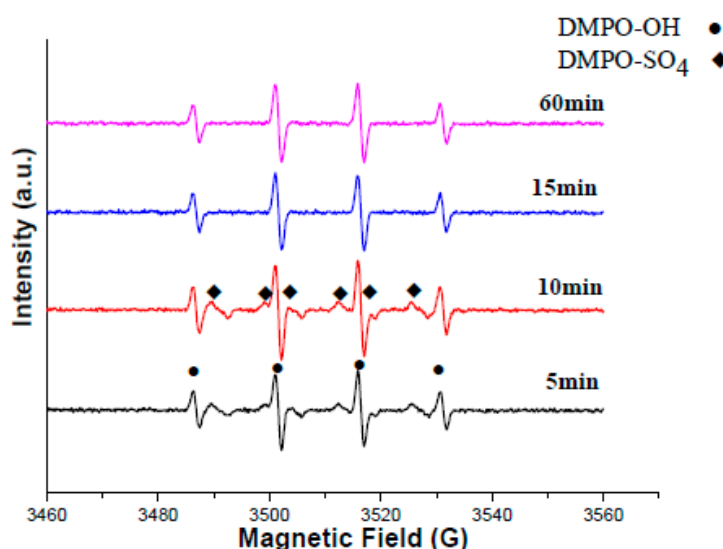


**Figure 7.** Electron paramagnetic resonance spectroscopy (EPR) spectra of PDS activation with EG.  $[AR97]_0 = 50 \text{ mg} \times \text{L}^{-1}$ ;  $[PDS]_0 = 2 \text{ mmol} \times \text{L}^{-1}$ ;  $[EG2]_0 = 1 \text{ g} \times \text{L}^{-1}$ ;  $\text{pH} = 6.9$ .

### 2.9. Verification of Method Reproducibility by Commercial Expandable Graphite

We performed experiments with commercial expandable graphite (Qingdao Tianhe graphite Co., Ltd., Qingdao, China) to verify the method reproducibility. The commercial expandable graphite expanded at 300, 600 and 800 °C to obtain the expanded graphite, and the products were defined as EG1', EG2' and EG3', respectively. Figure S5 depicts the adsorptive and catalytic performances of different EG samples by AR97 removal. Within 80 min, only 8.1, 14.6 and 30.1% AR97 were adsorbed by the EG1', EG2' and EG3', respectively. As shown in Figure 3a, 2.4% AR97 was oxidized by the sole PDS system. However, 21.6, 85.3 and 97.5% AR97 were degraded by the PDS/EG1', PDS/EG2' and PDS/EG3' combined system, respectively. Therefore, it was obvious that there was a remarkable synergistic effect in the PDS/EG2' and PDS/EG3' combined system. This result was consistent with those of the previous experiments, and the reproducibility of the EG/PDS combined system was confirmed. It also testified the importance of expansion temperature for preparing expanded graphite from expandable graphite.

## 3. Materials and Methods

### 3.1. Materials

Acid Red 97, (mol wt 698.6; C.I. No.:10169-02-5) (Figure S1) was supplied by Hebei Dingzhou Arpino LCD Material Co. Ltd. (Baoding, China). Sodium peroxydisulfate ( $\text{Na}_2\text{S}_2\text{O}_8$ , PDS containing 99.99%) was purchased from Shanghai Aladdin industrial corporation (Shanghai, China). All the other reagents were of A.R. grade. Natural flake graphite (FG) was purchased from Qingdao Tianhe graphite Co., Ltd.

MWCNTs (purity  $\geq 95\%$ , length 0.5–2  $\mu\text{m}$ , Outside Diameter 30–50 nm, SSA:  $>60 \text{ m}^2 \times \text{g}^{-1}$ ) was supplied by Nanjing XFNANO Materials Tech Co., Ltd. (Nanjing, China) and used without further processes. Reduced graphene oxide (purity  $> 98\%$ , layers  $< 10$ , SSA:  $500\text{--}1000 \text{ m}^2 \times \text{g}^{-1}$ ) was supplied by Chengdu Organic Chemicals Co., Ltd. (Chengdu, China) and used without further processes.

### 3.2. Preparation of the Expanded Graphites

10 g flake graphite was added to 30 mL 70% H<sub>2</sub>SO<sub>4</sub>, then 1.0 g potassium permanganate was added slowly under constant stirring. The mixture was stirred for 1 hour at an ambient temperature to make it fully react. The acidified graphite was washed with deionized water to pH 6–7. 4 mL, fuming nitric acid was mixed with 10 g acidified graphite, and then 2 mL acetic acid and 3 mL formic acid were dripped into the mixture of graphite with continuous stirring. After a 1-hour reaction, the product was washed and dried to obtain the expandable graphite. The expandable graphite expanded at 300, 600 and 800 °C to obtain the expanded graphite, and the products were defined as EG1, EG2 and EG3, respectively.

### 3.3. Catalytic Degradation Experimental and Analytical Methods

All experiments were performed at an ambient temperature (20 ± 1 °C). PDS and EG were added simultaneously into the AR97 solution (100 mL, 50 mg × L<sup>-1</sup>) at the beginning of each experiment. Experiments were performed at pH 6.9, which resulted from the dissolution of AR 97 in deionized water without further adjustment. When the effect of pH was explored, the pH of the solution was adjusted by using H<sub>2</sub>SO<sub>4</sub> or NaOH aqueous solutions. Figure 8 illustrates the scheme of the experimental procedure and apparatus. To investigate the stability of EG, EG was collected after each reaction, washed with water, and dried for reuse. The passivated catalysts after the second run were regenerated by annealing in a muffle furnace at 600 °C for about 10 seconds and cooled naturally.

The decolorization of AR97 solution was monitored by measuring the maximum absorbance at λ = 497 nm with a Shimadzu UV2501 spectrophotometer (Tokyo, Japan). The AR97 removal ratio is calculated in Equation (9):

$$\text{degradation efficiency} = (1 - C_t/C_0) \times 100\% \quad (9)$$

$$\ln(C_0/C_t) = k_{\text{obs}}t \quad (10)$$

The initial first-order rate constant, *k*, was obtained by Equation (10), where C<sub>t</sub> and C<sub>0</sub> were the AR97 concentration at time *t* and the initial concentration, respectively.

The concentration of PDS was determined by the KI spectrophotometric method [62]. The free radicals were detected by EPR on a Bruker A300 spectrometer (Karlsruhe, Germany) with 5,5-Dimethyl-1-pyrroline-*N*-oxide (DMPO) as a spin-trapping reagent. Each experiment was carried out at least twice, and the data quoted in this paper is the mean value (<5% variance).

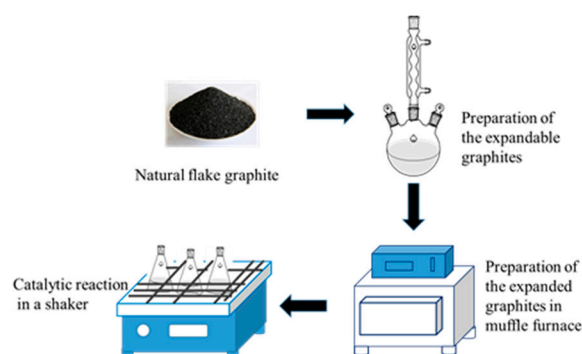


Figure 8. Schematic illustration of the experimental apparatus and procedure.

### 3.4. Characterization of EG

FTIR spectrum of the material was recorded on a Shimadzu IR Prestige-21 FTIR Spectrometer. XPS was recorded by a Thermo ESCALAB 250 (Thermo Fisher Scientific, Waltham, MA, USA), using Al-Kα excitation radiation (1486.6 eV). Raman spectra was acquired on a Horiba (LabRam-HR) Raman spectrometer (Paris, France) using argon ion laser source with λ at 514 nm. X-ray diffraction (XRD)

pattern was obtained on a TD-300 (Dandong Tongda Science and Technology Co., Ltd., Dandong, China) diffractometer system using Cu-K $\alpha$  radiation. The morphology of EG was examined using SEM (KYKY-EM3900M, KYKY Technology Co., Ltd., Beijing, China). Contact angle for water droplets on the surface of EG was measured with contact angle meter (SDC-200S, Sindin Precision Instruments Co., Ltd., Dongguan, China). The pH<sub>pzc</sub> (point of zero charge) of the samples were evaluated by dispersing 250 mg of EG samples into four milliliters of CO<sub>2</sub>-free water at 25 °C [63].

#### 4. Conclusions

In summary, expanded graphite was prepared and proposed for the new application as catalysts for activating PDS. The experiment results have demonstrated that the catalytic performance of these EG samples were significantly influenced by the expansion temperature, as the sample treated at 600 °C (EG2) showed the best catalytic capability. The Raman characterizations suggested that EG samples had high order and integrity. Compared with other catalysts, EG has a lower functional group content but has more sp<sup>2</sup> carbon, so sp<sup>2</sup> carbon structure may be the main active sites in catalytic reaction. The degradation efficiency of AR97 increased with raising the PDS dosage and the EG loadings. The pH of aqueous solution played an important role in degradation and adsorption, and near-neutrality was the optimal pH in this research. The results of quenching tests suggested that the radical pathway played a critical role in the dye degradation. The decolorization of AR97 dominantly occurred on the surface of EG, rather than the bulk solution. The radicals oxidation mechanism was further confirmed by electron paramagnetic resonance spectroscopy. Although the efficiencies of AR97 removal in the EG reuse test obviously decreased, the EG sample could be regenerated by annealing, and the catalytic ability was almost fully recovered. The reproducibility of the EG/PDS combined system for the oxidation of AR97 was confirmed by commercial expandable graphite. This study provides a green, low-cost, and efficient catalyst for environmental remediation.

**Supplementary Materials:** The following are available online at <http://www.mdpi.com/2073-4344/9/3/280/s1>, Figure S1: Chemical structure of AR97. Figure S2: SEM pictures of EG (a), EG after reaction (b), N<sub>2</sub> sorption isotherms (c), and pore size distributions of the EG samples (d). Figure S3: XRD patterns of EG. Figure S4: Contact angle measurement diagram of EG. Figure S5: The removal of AR97 under different EG'. Table S1: Elemental compositions and textural properties of the EG samples. Table S2: Langmuir isothermal adsorption equations of AR 97 to EG. Table S3: Freundlich isothermal adsorption equations of AR 97 to EG.

**Author Contributions:** R.L. designed the experiments; R.L. performed the experiments and analyzed the data; W.S. contributed reagents and analysis tools; R.L. wrote the paper. The manuscript was written by R.L. and edited by W.S. and J.L.

**Funding:** The authors would like to thank the foundation of Langfang Normal University (LSBS201302) for financial grant. The authors also thank the Foundation of Hebei Education Department (QN2015206).

**Conflicts of Interest:** The authors declare no conflict of interest.

#### References

1. Oh, W.D.; Dong, Z.; Lim, T.T. Generation of sulfate radical through heterogeneous catalysis for organic contaminants removal: Current development, challenges and prospects. *Appl. Catal. B Environ.* **2016**, *194*, 169–201. [CrossRef]
2. Bouchard, J.; Maine, C.; Argyropoulos, D.S.; Berry, R.M. Kraft Pulp Bleaching Using In-situ Dimethyldioxirane: Mechanism and Reactivity of the Oxidants. *Holzforchung—Int. J. Biol. Chem. Phys. Technol. Wood* **1998**, *52*, 499–505.
3. Wang, S. A Comparative study of Fenton and Fenton-like reaction kinetics in decolourisation of wastewater. *Dyes Pigm.* **2008**, *76*, 714–720. [CrossRef]
4. Hammouda, S.B.; Zhao, F.; Safaei, Z.; Srivastava, V.; Ramasamy, D.L.; Iftekhar, S.; Kalliola, S.; Sillanpää, M. Degradation and mineralization of phenol in aqueous medium by heterogeneous monopersulfate activation on nanostructured cobalt based-perovskite catalysts ACoO<sub>3</sub> (A = La, Ba, Sr and Ce): Characterization, kinetics and mechanism study. *Appl. Catal. B Environ.* **2017**, *215*, 60–73. [CrossRef]

5. Tan, C.; Gao, N.; Chu, W.; Li, C.; Templeton, M.R. Degradation of diuron by persulfate activated with ferrous ion. *Sep. Purif. Technol.* **2012**, *95*, 44–48. [[CrossRef](#)]
6. Li, H.; Guo, J.; Yang, L.; Lan, Y. Degradation of methyl orange by sodium persulfate activated with zero-valent zinc. *Sep. Purif. Technol.* **2014**, *132*, 168–173. [[CrossRef](#)]
7. Li, Y.; Li, H.; Zhang, J.; Quan, G.; Lan, Y. Efficient Degradation of Congo Red by Sodium Persulfate Activated with Zero-Valent Zinc. *Water Air Soil Pollut.* **2014**, *225*, 2121–2128. [[CrossRef](#)]
8. Rodriguez, S.; Vasquez, L.; Romero, A.; Santos, A. Dye Oxidation in Aqueous Phase by Using Zero-Valent Iron as Persulfate Activator: Kinetic Model and Effect of Particle Size. *Ind. Eng. Chem. Res.* **2014**, *53*, 12288–12294. [[CrossRef](#)]
9. Wang, Y.; Xie, Y.; Chen, C.; Duan, X.; Sun, H.; Wang, S. Synthesis of Magnetic Carbon Supported Manganese Catalysts for Phenol Oxidation by Activation of Peroxymonosulfate. *Catalysts* **2017**, *7*, 3. [[CrossRef](#)]
10. Stoia, M.; Muntean, C.; Militaru, B. MnFe<sub>2</sub>O<sub>4</sub> nanoparticles as new catalyst for oxidative degradation of phenol by peroxydisulfate. *J. Environ. Sci. China* **2017**, *53*, 269–277. [[CrossRef](#)]
11. Zhao, Y.S.; Sun, C.; Sun, J.Q.; Zhou, R. Kinetic modeling and efficiency of sulfate radical-based oxidation to remove p-nitroaniline from wastewater by persulfate/Fe<sub>3</sub>O<sub>4</sub> nanoparticles process. *Sep. Purif. Technol.* **2015**, *142*, 182–188. [[CrossRef](#)]
12. Wang, Y.; Indrawirawan, S.; Duan, X.; Sun, H.; Ang, H.M.; Tadé, M.O.; Wang, S. New insights into heterogeneous generation and evolution processes of sulfate radicals for phenol degradation over one-dimensional  $\alpha$ -MnO<sub>2</sub> nanostructures. *Chem. Eng. J.* **2015**, *266*, 12–20. [[CrossRef](#)]
13. Saputra, E.; Muhammad, S.; Sun, H.; Wang, S. Activated carbons as green and effective catalysts for generation of reactive radicals in degradation of aqueous phenol. *RSC Adv.* **2013**, *3*, 21905–21910. [[CrossRef](#)]
14. Duan, X.; Sun, H.; Kang, J.; Wang, Y.; Indrawirawan, S.; Wang, S. Insights into Heterogeneous Catalysis of Persulfate Activation on Dimensional-Structured Nanocarbons. *ACS Catal.* **2015**, *5*, 4629–4636. [[CrossRef](#)]
15. Chen, H.; Carroll, K.C. Metal-free catalysis of persulfate activation and organic-pollutant degradation by nitrogen-doped graphene and aminated graphene. *Environ. Pollut.* **2016**, *215*, 96–102. [[CrossRef](#)]
16. Sun, H.; Liu, S.; Zhou, G.; Ang, H.M.; Tadé, M.O.; Wang, S. Reduced graphene oxide for catalytic oxidation of aqueous organic pollutants. *ACS Appl. Mater. Interfaces* **2012**, *4*, 5466–5471. [[CrossRef](#)]
17. Xin, C.; Guo, H.; Zhang, Y.; Xiao, W.; Yang, L. Non-photochemical production of singlet oxygen via activation of persulfate by carbon nanotubes. *Water Res.* **2017**, *113*, 80–88.
18. Lee, H.; Lee, H.J.; Jeong, J.; Lee, J.; Park, N.B.; Lee, C. Activation of persulfates by carbon nanotubes: Oxidation of organic compounds by nonradical mechanism. *Chem. Eng. J.* **2015**, *266*, 28–33. [[CrossRef](#)]
19. Duan, X.; Su, C.; Zhou, L.; Sun, H.; Suvorova, A.; Odedairo, T.; Zhu, Z.; Shao, Z.; Wang, S. Surface controlled generation of reactive radicals from persulfate by carbocatalysis on nanodiamonds. *Appl. Catal. B Environ.* **2016**, *194*, 7–15. [[CrossRef](#)]
20. Matzek, L.W.; Carter, K.E. Activated persulfate for organic chemical degradation: A review. *Chemosphere* **2016**, *151*, 178–188. [[CrossRef](#)]
21. Wang, J.; Wang, S. Activation of persulfate (PS) and peroxymonosulfate (PMS) and application for the degradation of emerging contaminants. *Chem. Eng. J.* **2018**, *334*, 1502–1517. [[CrossRef](#)]
22. Wu, Y.; Guo, J.; Han, Y.; Zhu, J.; Zhou, L.; Lan, Y. Insights into the mechanism of persulfate activated by rice straw biochar for the degradation of aniline. *Chemosphere* **2018**, *200*, 373–379. [[CrossRef](#)] [[PubMed](#)]
23. Kang, J.; Duan, X.; Wang, C.; Sun, H.; Tan, X.; Tade, M.O.; Wang, S. Nitrogen-doped bamboo-like carbon nanotubes with Ni encapsulation for persulfate activation to remove emerging contaminants with excellent catalytic stability. *Chem. Eng. J.* **2018**, *332*, 398–408. [[CrossRef](#)]
24. Liu, N.; Zhang, L.; Xue, Y.; Lv, J.; Yu, Q.; Yuan, X. Nitrogen-Doped Carbon Material as a Catalyst for the Degradation of Direct Red23 based on Persulfate Oxidation. *Sep. Purif. Technol.* **2017**, *184*, 213–219. [[CrossRef](#)]
25. Guo, Y.; Zeng, Z.; Zhu, Y.; Huang, Z.; Cui, Y.; Yang, J. Catalytic oxidation of aqueous organic contaminants by persulfate activated with sulfur-doped hierarchically porous carbon derived from thiophene. *Appl. Catal. B Environ.* **2018**, *220*, 635–644. [[CrossRef](#)]
26. Chung, D.D.L. A review of exfoliated graphite. *J. Mater. Sci.* **2016**, *51*, 554–568. [[CrossRef](#)]
27. Raulo, A.; Suin, S.; Paria, S.; Khatua, B.B. Expanded graphite (EG) as a potential filler in the reduction of percolation threshold of multiwall carbon nanotubes (MWCNT) in the PMMA/HDPE/EG/MWCNT nanocomposites. *Polym. Compos.* **2016**, *37*, 2070–2082. [[CrossRef](#)]

28. Lee, J.H.; Kim, S. The determination of the adsorption performance of graphite for VOCs and formaldehyde. *Energy Build.* **2012**, *46*, 56–61. [[CrossRef](#)]
29. Hanifah, M.F.R.; Jaafar, J.; Aziz, M.; Ismail, A.F.; Rahman, M.A.; Othman, M.H.D. Synthesis of Graphene Oxide Nanosheets via Modified Hummers' Method and Its Physicochemical Properties. *J. Teknol.* **2015**, *74*, 195–198. [[CrossRef](#)]
30. Bradder, P.; Ling, S.K.; Wang, S.; Liu, S. Dye Adsorption on Layered Graphite Oxide. *J. Chem. Eng. Data* **2011**, *56*, 138–141. [[CrossRef](#)]
31. Jr, W.S.H.; Offeman, R.E. Preparation of Graphitic Oxide. *J. Am. Chem. Soc.* **1958**, *80*, 1339.
32. Duan, X.; Sun, H.; Ao, Z.; Zhou, L.; Wang, G.; Wang, S. Unveiling the active sites of graphene-catalyzed peroxymonosulfate activation. *Carbon* **2016**, *107*, 371–378. [[CrossRef](#)]
33. Park, S.J.; Lee, S.Y.; Kim, K.S.; Jin, F.L. A novel drying process for oil adsorption of expanded graphite. *Carbon Lett.* **2013**, *14*, 193–195. [[CrossRef](#)]
34. Zhao, Y.H.; Jin, C.; Deng-Xin, L.I. Adsorption of Cr (VI) in Wastewater on Expanded Graphite. *Environ. Sci. Technol.* **2012**, *35*, 149–152.
35. Li, J.T.; Song, Y.L.; Meng, X.Y.; Liu, C.M. Decolourization of C.I. Direct blue 78 aqueous solution in presence of exfoliated graphite under ultrasound irradiation. *Indian J. Chem. Technol.* **2009**, *16*, 411–416.
36. Poh, H.L.; Sanek, F.; Ambrosi, A.; Zhao, G.; Sofer, Z.; Pumera, M. Graphenes prepared by Staudenmaier, Hofmann and Hummers methods with consequent thermal exfoliation exhibit very different electrochemical properties. *Nanoscale* **2012**, *4*, 3515–3522. [[CrossRef](#)]
37. Peng, T.; Liu, B.; Gao, X.; Luo, L.; Sun, H. Preparation, Quantitative Surface Analysis, Intercalation Characteristics and Industrial Implications of Low Temperature Expandable Graphite. *Appl. Surf. Sci.* **2018**, *444*, 800–810. [[CrossRef](#)]
38. Shi, P.; Su, R.; Zhu, S.; Zhu, M.; Li, D.; Xu, S. Supported cobalt oxide on graphene oxide: highly efficient catalysts for the removal of Orange II from water. *J. Hazard. Mater.* **2012**, *229–230*, 331–339. [[CrossRef](#)]
39. Hassouna, F.; Laachachi, A.; Chapron, D.; Mouedden, Y.E.; Toniazzo, V.; Ruch, D. Development of new approach based on raman spectroscopy to study the dispersion of expanded graphite in poly (lactide). *Polym. Degrad. Stab.* **2011**, *96*, 2040–2047. [[CrossRef](#)]
40. Tang, L.; Liu, Y.; Wang, J.; Zeng, G.; Deng, Y.; Dong, H.; Feng, H.; Wang, J.; Peng, B. Enhanced activation process of persulfate by mesoporous carbon for degradation of aqueous organic pollutants: Electron transfer mechanism. *Appl. Catal. B Environ.* **2018**, *231*, 1–10. [[CrossRef](#)]
41. Vermisoglou, E.C.; Giannakopoulou, T.; Romanos, G.E.; Boukos, N.; Giannouri, M.; Lei, C.; Lekakou, C.; Trapalis, C. Non-activated high surface area expanded graphite oxide for supercapacitors. *Appl. Surf. Sci.* **2015**, *358*, 110–121. [[CrossRef](#)]
42. Pang, X.Y.; Tian, Y.; Weng, M.Q. Preparation of expandable graphite with silicate assistant intercalation and its effect on flame retardancy of ethylene vinyl acetate composite. *Polym. Compos.* **2015**, *36*, 1407–1416. [[CrossRef](#)]
43. Wang, H.; Zhao, Y.; Lekuan, M.A.; Fan, P.; Congbin, X.U.; Jiao, C.; Lin, A. Preparation of Composite Modified Expanded Graphite and Its Adsorption on Acid Brilliant Blue Dye. *Chem. J. Chin. Univ.* **2016**, *37*, 335–341.
44. Yang, S.; Li, L.; Xiao, T.; Zhang, Y.; Zheng, D. Promoting effect of ammonia modification on activated carbon catalyzed peroxymonosulfate oxidation. *Sep. Purif. Technol.* **2016**, *160*, 81–88. [[CrossRef](#)]
45. Zhang, J.; Shao, X.; Shi, C.; Yang, S. Decolorization of Acid Orange 7 with peroxymonosulfate oxidation catalyzed by granular activated carbon. *Chem. Eng. J.* **2013**, *232*, 259–265. [[CrossRef](#)]
46. Yang, S.; Yang, X.; Shao, X.; Niu, R.; Wang, L. Activated carbon catalyzed persulfate oxidation of Azo dye acid orange 7 at ambient temperature. *J. Hazard. Mater.* **2011**, *186*, 659–666. [[CrossRef](#)]
47. Wang, Y.; Ao, Z.; Sun, H.; Duan, X.; Wang, S. Activation of peroxymonosulfate by carbonaceous oxygen groups: Experimental and density functional theory calculations. *Appl. Catal. B Environ.* **2016**, *198*, 295–302. [[CrossRef](#)]
48. Li, M.; Hsieh, T.C.; Doong, R.A.; Huang, C.P. Tuning the adsorption capability of multi-walled carbon nanotubes to polar and non-polar organic compounds by surface oxidation. *Sep. Purif. Technol.* **2013**, *117*, 98–103. [[CrossRef](#)]
49. Wu, W.; Chen, W.; Lin, D.; Yang, K. Influence of surface oxidation of multiwalled carbon nanotubes on the adsorption affinity and capacity of polar and nonpolar organic compounds in aqueous phase. *Environ. Sci. Technol.* **2012**, *46*, 5446–5454. [[CrossRef](#)]

50. Liu, Z.; Zeng, Z.; Yang, J.; Cui, Y.; Wu, A.; Li, Z.; Huang, Z. Degradation of Phenol with Persulfate Activated by Surface Modified Activated Carbon. *Chem. J. Chin. Univ.* **2017**, *38*, 1241–1248.
51. Yu, X.; Bao, Z.; Barker, J.R. Free Radical Reactions Involving  $\text{Cl}$ ,  $\text{Cl}_2\cdot^-$  and  $\text{SO}_4\cdot^-$  in the 248 nm Photolysis of Aqueous Solutions Containing  $\text{S}_2\text{O}_8^{2-}$  and  $\text{Cl}^-$ . *J. Phys. Chem. A* **2004**, *108*, 295–308. [[CrossRef](#)]
52. Wang, Z.M.; Huang, T.Y.; Chen, J.B.; Li, W.W.; Zhang, L.M. Degradation of Acid Orange 7 with Persulfate Activated by Silver Loaded Granular Activated Carbon. *Environ. Sci.* **2015**, *36*, 4127–4134.
53. Georgi, A.; Kopinke, F.D. Interaction of adsorption and catalytic reactions in water decontamination processes: Part I. Oxidation of organic contaminants with hydrogen peroxide catalyzed by activated carbon. *Appl. Catal. B Environ.* **2005**, *58*, 9–18. [[CrossRef](#)]
54. Duan, X.; Sun, H.; Wang, Y.; Kang, J.; Wang, S. N-Doping-Induced Nonradical Reaction on Single-Walled Carbon Nanotubes for Catalytic Phenol Oxidation. *ACS Catal.* **2015**, *5*, 553–559. [[CrossRef](#)]
55. Buxton, G.V.; Greenstock, C.L.; Helman, W.P.; Ross, A.B. Critical Review of rate constants for reactions of hydrated electrons, hydrogen atoms and hydroxyl radicals ( $\cdot\text{OH}/\cdot\text{O}^-$ ) in Aqueous Solution. *J. Phys. Chem. Ref. Data* **1988**, *17*, 513–886. [[CrossRef](#)]
56. And, M.E.L.; Tarr, M.A. Inhibition of Hydroxyl Radical Reaction with Aromatics by Dissolved Natural Organic Matter. *Environ. Sci. Technol.* **2000**, *34*, 444–449.
57. Ziajka, J.; Pasiuk-Bronikowska, W. Rate constants for atmospheric trace organics scavenging  $\text{SO}_4\cdot^-$  in the Fe-catalysed autoxidation of S (IV). *Atmos. Environ.* **2005**, *39*, 1431–1438. [[CrossRef](#)]
58. Li, S.; Tian, S.; Feng, Y.; Lei, J.; Wang, P.; Xiong, Y. A comparative investigation on absorption performances of three expanded graphite-based complex materials for toluene. *J. Hazard. Mater.* **2010**, *183*, 506–511. [[CrossRef](#)]
59. Ling, Z.; Yong, W.; Jin, S.W.; Lu, Q.Z.; Jiang, J. Adsorption isotherm, kinetic and mechanism of expanded graphite for sulfadiazine antibiotics removal from aqueous solutions. *Environ. Technol.* **2017**, *38*, 1–10.
60. Pang, X.Y.; Lv, P.; Feng, Y.Q.; Liu, X. Study on the adsorbing characteristics of expanded graphite for organic dyes. *Environ. Sci.* **2008**, *3*, 150–157.
61. Ouyang, D.; Yan, J.; Qian, L.; Chen, Y.; Han, L.; Su, A.; Zhang, W.; Ni, H.; Chen, M. Degradation of 1,4-dioxane by biochar supported nano magnetite particles activating persulfate. *Chemosphere* **2017**, *184*, 609–617. [[CrossRef](#)]
62. Liang, C.; Huang, C.F.; Mohanty, N.; Kurakalva, R.M. A rapid spectrophotometric determination of persulfate anion in ISCO. *Chemosphere* **2008**, *73*, 1540–1543. [[CrossRef](#)]
63. Morales-Torres, S.; Silva, A.M.T.; Maldonado-Hódar, F.J.; Machado, B.F.; Pérez-Cadenas, A.F.; Faria, J.L.; Figueiredo, J.L.; Carrasco-Marín, F. Pt-catalysts supported on activated carbons for catalytic wet air oxidation of aniline: Activity and stability. *Appl. Catal. B Environ.* **2011**, *105*, 86–94. [[CrossRef](#)]

